remote sensing

MDPI

Article

GNSS Horizontal Motion Field in the Beijing Plain in View of The Variation Characteristics of The 3D Deformation Field

Jun Wang [1], Shunqiang Hu [2], Tan Wang [1,3], Hong Liang [4] and Zhenyu Yang [1,*]

[1] College of Resource Environment and Tourism, Capital Normal University, Beijing 100048, China
[2] Department of Earth and Space Sciences, Southern University of Science and Technology, Shenzhen 518055, China
[3] China Earthquake Networks Center, Beijing 100045, China
[4] Meteorological Observation Center, China Meteorological Administration, Beijing 100081, China
* Correspondence: zhenyu.yang@cnu.edu.cn

Abstract: In view of the fact that there is no unified understanding of the GNSS horizontal velocity field in the Beijing Plain and the serious land subsidence in this area, we collected GNSS data from 2011 to 2021 and Sentinel 1A data from 2017 to 2021 and conducted high-precision GNSS data processing and PS-InSAR verification in order to determine the reason for the differences in the GNSS horizontal velocity field in the Beijing Plain. The results show that, under the stable Eurasian framework, the horizontal velocity of GNSS stations in the Beijing Plain is significantly inconsistent. The velocity of all GNSS stations ranged from −1.32 to 10.41 mm/yr in the E component and from −8.83 to 3.00 mm/yr in the N component. From 2011 to 2021, there was significant uneven land subsidence in the Beijing Plain, and the maximum land subsidence rate from 2017 to 2021 reached 107 mm/yr. In analyzing the observation data of the GNSS and InSAR, we conclude that the land subsidence in the Beijing Plain will indeed affect the GNSS horizontal velocity field in the subsidence area. Under the EURA_I08 reference framework, the horizontal deformation field in the Beijing Plain is mainly caused by the tectonic activity-derived overall SEE-direction movement, accompanied by the velocity field anomaly caused by local land subsidence.

Keywords: GNSS; PS-InSAR; land subsidence; velocity field; Beijing Plain

Citation: Wang, J.; Hu, S.; Wang, T.; Liang, H.; Yang, Z. GNSS Horizontal Motion Field in the Beijing Plain in View of The Variation Characteristics of The 3D Deformation Field. *Remote Sens.* **2023**, *15*, 787. https://doi.org/10.3390/rs15030787

Academic Editor: Giuseppe Casula

Received: 27 December 2022
Revised: 18 January 2023
Accepted: 25 January 2023
Published: 30 January 2023

1. Introduction

The Global Navigation Satellite System (GNSS) velocity field has been widely used for earth reference frame establishment and maintenance [1–3], plate tectonic motion [4–8], and earthquake mechanism [9–13] determination. Therefore, it is of great significance to obtain an accurate and reliable GNSS velocity field in a given region for geodynamic and geodesy research. In recent years, with the development of GNSS technology, a large number of GNSS observation station networks have been established in Beijing, which mainly include the crustal movement observation network of China (CMONOC), the north China region/capital area project, the Beijing Global Satellite Positioning Integrated Application Service System (Beijing CORS), the meteorological observation station built by the Beijing Meteorological Bureau, and the Beijing land subsidence monitoring network. Based on these GNSS data, numerous scholars have studied the three-dimensional crustal deformation in the Beijing region. Shen et al. [14] used the observation data of 68 regional stations to investigate the crustal deformation in the North China/capital circle region, and their results showed that the east-central area of mainland China was moving in the southeast-east direction at a rate of 8–11 mm/yr. Wu et al. [15] used GNSS data spanning from 2010 to 2014 in Beijing and the surrounding area, derived from CMONOC, and showed that the GNSS velocity field has no uniform direction or magnitude of movement. Chen [16] obtained data from 163 continuous and campaign stations of the CMONOC from 1999 to 2007 and proposed that compared to the stable Eurasian framework—except

for some GNSS stations around Beijing and Tianjin, which moved east or northeast—the Zhangjiakou–Bohai fault zone and other stations in the adjacent area all moved in the southeast direction. Chen [17] investigated the crustal deformation in the Beijing region and showed that the north of the fault presents a westward motion component, while the south of the fault presents an eastward motion component, bounded by the Nankou–Sunhe fault in the Beijing region. Based on the integration of GNSS data from multiple sources in mainland China in the Eurasian framework, Wang and Shen [5] concluded that the GNSS velocity field displays a relatively uniform movement direction, and the dominant movement direction is SEE in the Beijing region (Figure 1b). Lei et al. [18] concluded that the GNSS velocity field is chaotic, and there is no uniform motion trend in the Beijing region based on 75 GNSS data spanning from 2013 to 2018 from land subsidence monitoring networks. Obviously, there are differences among the GNSS horizontal velocity field results for the Beijing region, based on previous studies. To better investigate the crustal deformation characteristic in the Beijing region, it is necessary to further research the reasons for the inconsistency in the GNSS velocity field in the Beijing region.

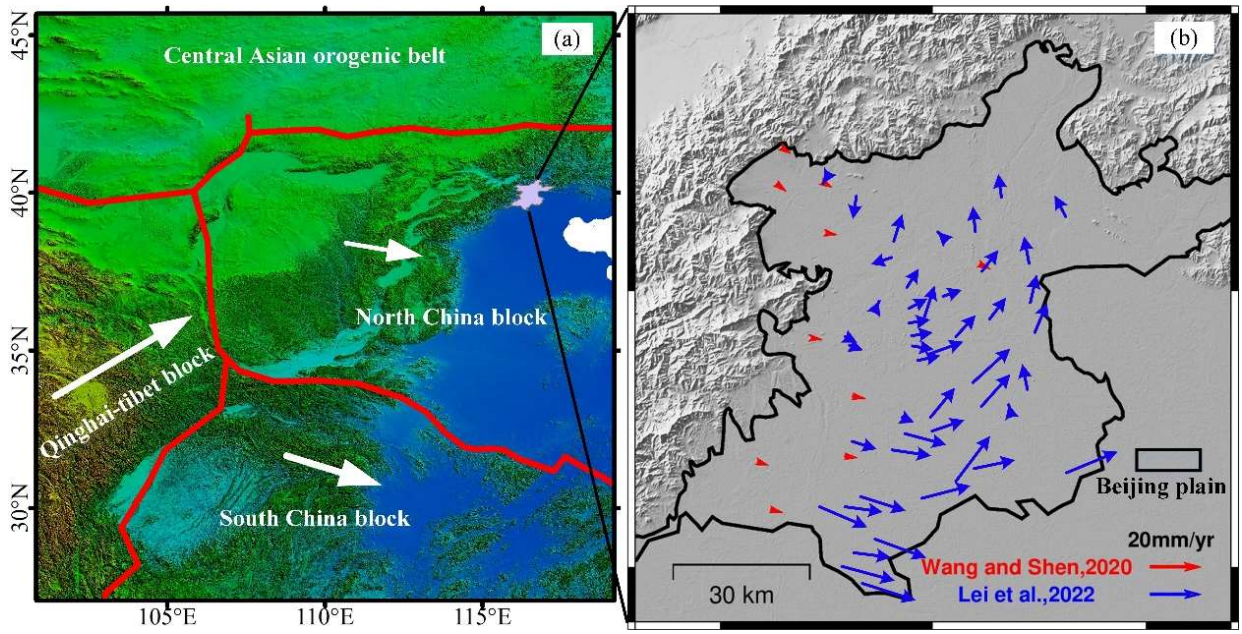

Figure 1. The tectonic plate positions of the Beijing Plain (**a**) and the GNSS horizontal velocity field in the Beijing Plain area (**b**) [5,18].

The presently active tectonics may be an important reason for the inconsistent GNSS velocity field in the Beijing Plain. However, land subsidence, as an environmental geological phenomenon of surface elevation loss [19], may also cause inconsistencies in the GNSS horizontal velocity field at the inter-annual scale. The land subsidence of the Beijing region was first discovered in 1935, located in the area from Xidan to Dongdan. With the development of land subsidence, the area with accumulated land subsidence of more than 50 mm accounted for 66% of the Beijing region until 2010 (up to 4200 km^2), and the largest accumulated subsidence reached 1233 mm [20]. The study of Cigna and Tapete [21] in Mexico City using InSAR technology showed that the motion rate of the study area was 0.3 cm/yr in the east–west direction as a whole; however, in the subsidence funnel area, an east–west deformation of 5 cm/yr was generated. Therefore, we investigated whether the GNSS horizontal velocity field is affected by land subsidence, based on the special geological background of serious land subsidence in the Beijing region.

A large number of studies have confirmed the feasibility of using GNSS technology to study surface vertical deformation. Sato et al. [22] concluded that a GNSS station displayed 7 cm of subsidence and uplift in winter and spring, respectively, every year in the city

of Kochigaya, Japan. Baldi et al. [23] studied land subsidence in the north-central Italian peninsula, and their results showed that the vertical accuracy can reach 3–4 mm according to the GNSS continuous operation reference stations. Hu et al. [4] used 27 GNSS position time series spanning from 2011 to 2020 to investigate the vertical crustal deformation in the Yunnan region, southwest China. Their results showed that the southwest Yunnan block was mainly subsidence (0.01–1.9 mm/yr), while the southern part of the Chuandian block was mainly uplift (0.13–2 mm/yr).

Synthetic aperture radar interferometry (InSAR) has been widely used in the field of surface deformation monitoring and has the advantages of high precision, low cost, and large measurement area. PS-InSAR technology, in particular, can well address the problems of atmospheric phase delay and incoherence and can also effectively obtain regional long time series and slowly changing deformation information. It has been successfully applied in Mexico [21], the North China Plain [24], and the southern Liaohe Plain [25]. However, as both GNSS and InSAR techniques are single-measurement methods, InSAR can not only cross-verify the GNSS-derived vertical deformation observations, such as the land subsidence studies of Lake Nasser in Egypt [26] and the Nile River [27], but it can also provide a basis for discussing how the land subsidence affects the horizontal velocity field in the subsidence area.

In view of the existing research on the inconsistent understanding of the GNSS horizontal velocity field in the Beijing Plain area and the geological background of serious land subsidence in the local area, the objective of this paper was to combine the GNSS and InSAR techniques to discuss whether land subsidence affects the regional GNSS horizontal velocity field in the Beijing Plain area.

2. GNSS Data and Processing

For this paper, the data of 21 GNSS continuous stations in the Beijing Plain area were collected from the International GNSS Service Organization (IGS), the Beijing Global Positioning Integrated Application Service System (Beijing CORS Stations), and the Beijing Meteorological Bureau, in the time span from 1st January 2011 to 15th May 2021. A detailed overview of the station data is shown in Table 1. In addition, we collected and collated the GNSS velocity field data for mainland China published by Wang and Shen [5] in 2020, among which there were 10 stations in the Beijing Plain. The detailed distribution of stations used in this paper is shown in Figure 2b, and the FTXF station from the Beijing Meteorological Bureau is shown in Figure 2c,d.

Table 1. GNSS station information.

Station	Base Type	Receiver Type	Antenna Type	Source
BJFS	shale	TRIMBLE NETR8	TRM59800.00	IGS
BJNM	limestone	SEPT POLARX3ETR	NOV702GG	IGS
CEHY	sandy	TRIMBLE NETR9	TRM29659.00	Beijing CORS
CHAO	sandy	TRIMBLE NETR9	TRM55971.00	Beijing CORS
DAXN	sandy	TRIMBLE NETR5	TRM41249.00	Beijing CORS
DSQI	sandy	TRIMBLE NETR8	TRM59800.00	Beijing CORS
NKYU	granite	TRIMBLE NETR9	TRM59800.00	Beijing CORS
NLSH	clay	TRIMBLE NETR9	TRM29659.00	Beijing CORS
PING	sandy	TRIMBLE NETR8	TRM59800.00	Beijing CORS
SHIJ	sandy	TRIMBLE NETR8	TRM59800.00	Beijing CORS
XIJI	sandy	TRIMBLE NETR5	TRM41249.00	Beijing CORS
CPXT	sandy	TPS LEGACY	TOPCR3_GGD	Beijing Meteorological Administration

Table 1. *Cont.*

Station	Base Type	Receiver Type	Antenna Type	Source
CYLG	sandy	TPS LEGACY	TOPCR3_GGD	Beijing Meteorological Administration
FSZF	clay	TPS LEGACY	TOPCR3_GGD	Beijing Meteorological Administration
FTXF	sandy	TPS LEGACY	TOPCR3_GGD	Beijing Meteorological Administration
HBZS	sandy	TPS LEGACY	TOPCR3_GGD	Beijing Meteorological Administration
HDBA	sandy	TPS LEGACY	TOPCR3_GGD	Beijing Meteorological Administration
LLHS	sandy	TPS LEGACY	TOPCR3_GGD	Beijing Meteorological Administration
SYSG	sandy	TPS LEGACY	TOPCR3_GGD	Beijing Meteorological Administration
TZMJ	sandy	TPS LEGACY	TOPCR3_GGD	Beijing Meteorological Administration
TZQX	sandy	TPS LEGACY	TOPCR3_GGD	Beijing Meteorological Administration

We used GAMIT/GLOBK10.71 software, developed by MIT, to calculate the baseline and network adjustment. In the GAMIT calculation process, the synchronous observation data of 16 IGS stations around China, including AIRA, CHAN, CHUM, DAEJ, GMSD, HYDE, IISC, IRKM, JFNG, KIT3, LHAZ, PIMO, POL2, SHAO, TASH, and TCMS, were combined and processed. The detailed calculation parameters used in our study are shown in Table 2. After the baseline solution was completed, the one-day relaxation solution was merged with the global solution h file (igs1-7) from the IGS data center. Then, GLOBK was used to carry out the network adjustment of the merged relaxation solution, and the original coordinate time series for each continuous station was obtained. In the GAMIT baseline solution results, the normalized root mean square error (NRMS) of the q file reflects the extent to which the baseline solution deviates from the weighted mean value of the baseline solution within a certain time span. The lower the NRMS value, the better the quality of the baseline solution; the NRMS value should be less than 0.3 under normal circumstances. The NRMS of the q file in the calculation results of this study was calculated, and its range was 0.17–0.22. Therefore, we believe that the quality of the baseline solution was high.

Due to the influence of receiver trouble, poor signal, or weather change, there were gross errors in the original coordinate time series. We used the 3IQR criterion to eliminate the gross errors. During long-term GNSS observations, the GNSS coordinate time series have step changes due to earthquakes, changes in the receiver and antenna, and so on. We used the least squares fitting method to correct the step changes of the three components of NEU. Accurate analysis of the noise in the coordinate time series can allow one to obtain more accurate GNSS calculation results and the movement trend of the reference station. Relevant studies have shown that for GNSS global solutions or regional network solutions with different time spans, white noise + flicker noise (WN + FN) provides an optimal noise model [28]. For this reason, Hector software was used to estimate the velocity and uncertainty of each measuring station under the WN + FN model.

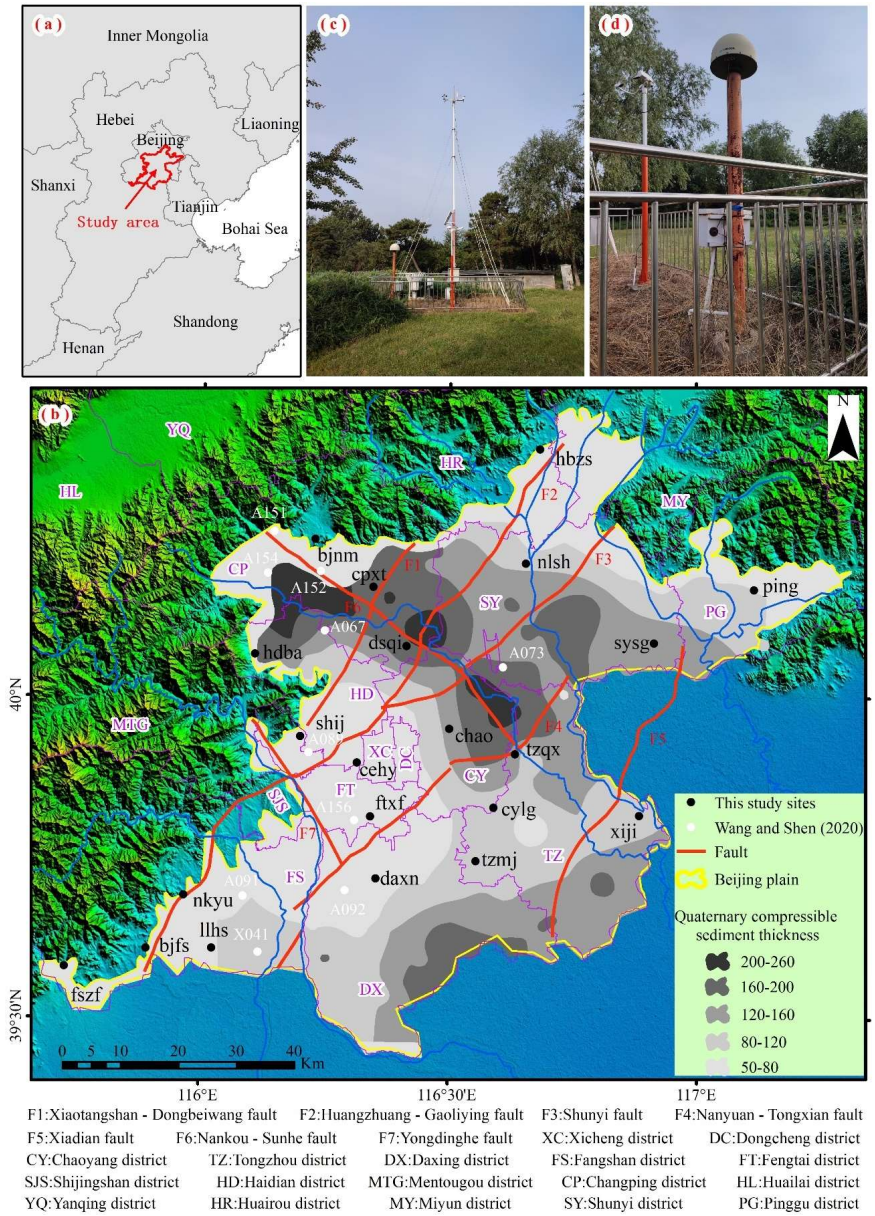

Figure 2. The distribution map of GNSS stations in the study area. Figure (**a**) is the geographical location of the study area, Figure (**b**) is the distribution of GNSS stations in the study area, and Figure (**c**,**d**) is the FTXF station.

In order to test the measurement accuracy of the GNSS continuous operation reference stations in the study area, the inner coincidence accuracy of each station was calculated. The results show that the median error of the E component at 21 continuous stations ranged from 0.18 to 1.73 mm/yr, with an average value of 0.49 mm/yr. The median error range of the N component was 0.16–1.43 mm/yr, with a mean value of 0.55 mm/yr. The median error range of the U component was 0.25–2.90 mm/yr, with a mean value of 1.24 mm/yr. This indicates that, due to the good observation environment of the continuous operation reference stations and the long time span of the observation data, each station had higher observation accuracy in all directions (i.e., N, E, and U), while the horizontal observation accuracy was obviously better than the vertical observation accuracy, which conforms to the existing understanding that the deformation monitoring accuracy in the vertical direction is 2–3 times lower than that in the horizontal direction [15].

Table 2. Main parameter settings of GAMIT.

Main Parameters	Solving Strategy
Interval of time	30 s
Satellite cutoff altitude angle	10°
Baseline processing mode	RELAX
Observed value	LC-AUTCLN
Ionospheric delay	The LC observation value was used to eliminate the ionospheric delay.
Tropospheric delay	The zenith dry delay was calculated by the GPT model. Zenith tropospheric delay is estimated every two hours and two NS and ES gradients are estimated daily.
Solar pressure model	SPHRC
Earth tide correction	IERS10
Ocean tide correction	FES2004
Atmospheric mapping function	VMF1
Coordinate reference frame	ITRF2014
GNSS measuring station constraints	(N, E, U) 30.00 m 30.00 m 30.00 m
IGS station constraint	(N, E, U) 0.025 m 0.025 m 0.025 m

3. Results

3.1. GNSS Monitoring Results

Based on the GNSS observation data from 2011 to 2021 for Beijing Plain, the surface deformation velocity field under the ITRF14 framework was obtained. As shown in Figure 3, under the ITRF14 framework, all GNSS stations had basically the same movement direction. Overall, they mainly moved in the SEE direction, which reflects the fact that the whole plain region has a unified continuous deformation feature under a continental dynamic environment. Among them, the velocity value of the E component of the GNSS stations calculated in this study ranged from 25.17 to 36.91 mm/yr, with an average value of 31.16 mm/yr. The velocity value of the N component ranged from −6.63 to −18.51 mm/yr, with an average value of −11.70 mm/yr. Finally, the velocity value of the U component ranged from −95.72 to 4.07 mm/yr, with an average value of −18.19 mm/yr. It can be seen that the velocity value of the U component varied greatly, reflecting the uneven subsidence characteristics in the Beijing Plain area. Under the ITRF framework, the monitoring results obtained in this study are consistent with the surface deformation status of the Beijing Plain area obtained by other scholars using GNSS technology [15,17,18].

The horizontal velocity field under the ITRF framework reflects the overall motion characteristics of the Beijing Plain under the global framework. This result can be considered the absolute motion velocity of each measuring station, based on the global benchmark. As the velocity field under the ITRF framework includes the horizontal motion velocity of the entire plate under the global reference frame and the horizontal strain generated within the region, and the horizontal motion component of the entire plate is large, it is difficult to determine the internal deformation of the region intuitively under the ITRF framework. In order to more accurately reflect the characteristics of the stress field inside the Beijing Plain, the velocity field under the ITRF framework was deduced using the overall velocity of the Eurasian plate in order to obtain the internal horizontal velocity field of all the stations relative to the stable Eurasian reference frame. In the calculation process, we used the Euler pole published by Altamimi et al. [29] (where the three parameters are −0.023060, −0.148300, and 0.208300 deg/Myr), in order to convert the velocity field under the ITRF framework to the EURA_I08 framework through GLOBK. In Figure 4, we can see that, compared to the stable Eurasian framework, the horizontal velocity values of each

GNSS station in the Beijing Plain decreased significantly, and the non-consistent changes were more obvious. After conversion, the value range of the E component was −1.32 to 10.41 mm/yr, and the velocity value of the N component was −8.83 to 3.00 mm/yr.

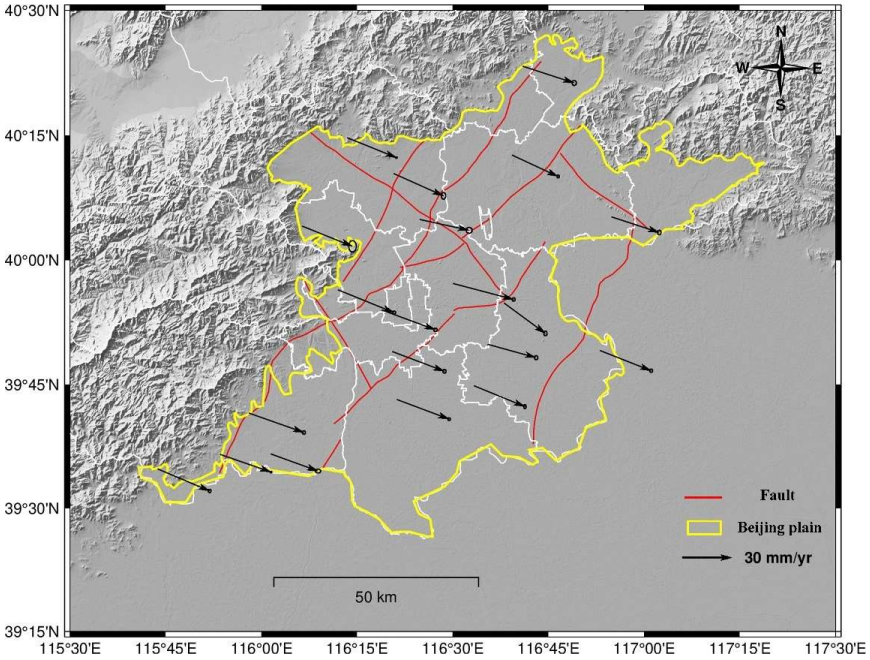

Figure 3. Velocity field under the ITRF14 framework. The grey background map represents the DEM-derived hill shade.

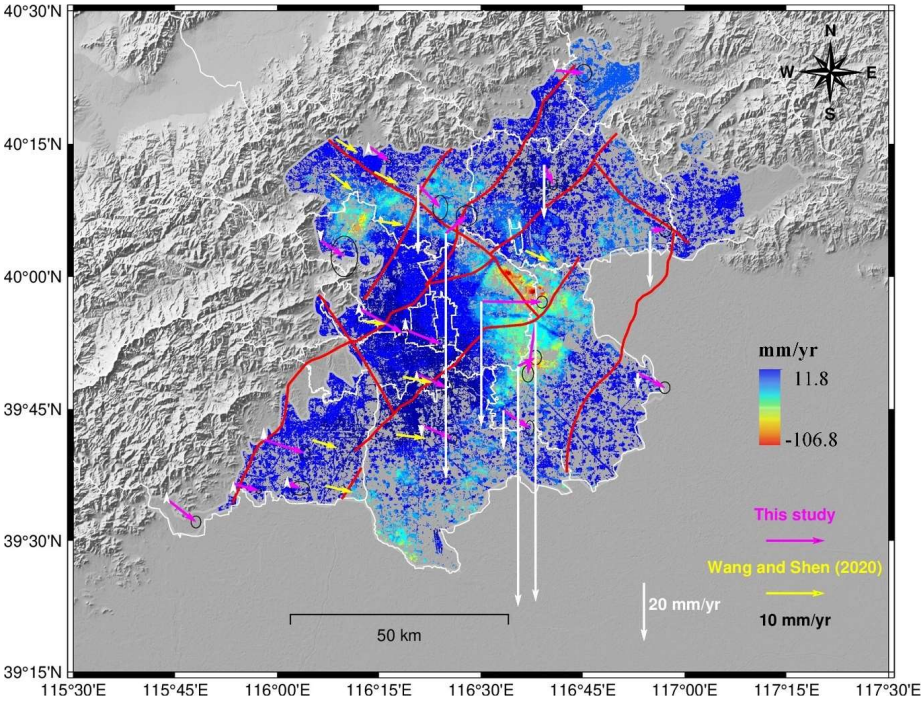

Figure 4. GNSS velocity field under the EURA_I08 framework and land subsidence rate map. The magenta and yellow vector arrows represent the GNSS velocity of this article and that of Wang and Shen (2020) [5], respectively. The white vector arrow represents the vertical velocity at the GNSS stations used in this study. The color base map represents the land subsidence field obtained by InSAR. The grey background map represents the DEM-derived hill shade.

We compared and analyzed the velocity field of Wang and Shen [5] under the EURA framework and found that these data presented a consistent motion direction (SEE direction), while the data obtained in our study present obvious inconsistent changes. When calculating the velocity field in mainland China, Wang and Shen [5] rejected the poor quality of the observation data (e.g., the observations made with GeoTracer receiver/antenna in 1999 and 2000) and the short time span of the data (<3 years in East China; <2 years in the western region) and considered that the stations had been disturbed by human activities (e.g., land subsidence caused by groundwater extraction, oil extraction, and coal mining in the North China Plain). The GNSS receivers/antennae used in this paper were all mainstream devices, such as Trimble or Topcon (Table 1; IGS station BJNM excluded), and the GNSS data time span was greater than 3 years. As shown in Figure 4, the stations with large differences in the GNSS horizontal velocity fields obtained in this paper were mainly distributed in Tongzhou, Chaoyang, Changping, Shunyi, and other typical historical subsidence areas. The fault activity affects the displacement field within the plate. In the horizontal direction, the strike-slip fault causes the horizontal motion velocity of the block on both sides of the fault to be inconsistent, while in the vertical direction, a normal fault or a thrust fault causes inconsistent vertical velocities on both sides of the fault. As the active fault rate in the Beijing Plain is usually less than 1 mm/yr [30], the local tectonic activity is not expected to cause such a huge difference in the horizontal velocity field of the GNSS. Therefore, land subsidence may be the cause of the inconsistent GNSS horizontal velocity. In order to verify the distribution characteristics of land subsidence in the Beijing Plain area in recent years and the accuracy of the GNSS vertical (U) component, we used PS-InSAR technology to further understand the land subsidence in the Beijing area.

3.2. Verification of GNSS Vertical U Component Results

Generally speaking, PS-InSAR technology requires at least 25 SAR images to perform reliable PS analysis [31]. We collected the ascending Sentinel-1A data (interference wide-frame, C-band) spanning from 20th May 2017 to 15th August 2021, of which the path was 142 and the frame was 126. The interval between each image was 36 days, a total of 44 radar images were finally selected, and the spatial baseline ranged from 5.04 to 128.39 m. We used SNAP and STAMPS software to process the PS-InSAR data [32–35], where the primary image date selected was 10th May 2019. We used the SRTM 90 m DEM to remove the terrain phase. When we used STAMPS processing, the amplitude dispersion was set to 0.4. Relevant studies have shown [36] that GACOS has a good effect on correcting the tropospheric delay in the interferogram in the Beijing Plain region, and, for deformation studies based on time series, the deformation results of InSAR and GNSS are most consistent after using GACOS for correction. Therefore, we used GACOS for atmospheric delay correction [37]. The base level origin of Yuyuantan in Beijing can be used as the elevation reference for land subsidence in Beijing [38], and was the reference point for InSAR deformation monitoring in our study. Finally, we used Equation (1) to convert LOS deformation into the vertical direction, and a surface vertical deformation rate chart in the study area was obtained (Figure 4).

$$V_{ver} = \frac{V_{Los}}{\cos(\theta)} \quad (1)$$

where the V_{ver} is the vertical deformation rate, V_{Los} is the LOS direction rate, and θ is the incident angle.

The PS-InSAR results demonstrate that the land subsidence of Chaoyang and Tongzhou in the eastern plain area was the most serious area in the Beijing region. Several major subsidence centers were in contiguous development, and the maximum annual subsidence rate reached 106.8 mm/yr. In the north of the plain, the land subsidence distribution was scattered, and the serious subsidence areas were mainly distributed in the south of Changping District, the north of Haidian District, and part of Shunyi. The serious land subsidence

in the southern plain area was mainly concentrated in Daxing District, especially in the border area with Hebei Province.

As the effective observation time span of the GNSS stations was inconsistent with the time span of the InSAR data, in order to truly compare the accuracy of the two monitoring results, we intercepted the data of the two observation means within the same time span, and finally chose three GNSS stations for comparison (to ensure the accuracy of the GNSS measurement results, the data time span of all GNSS stations was greater than 2.5 years). As the GNSS stations and the PS points selected by PS-InSAR technology did not coincide completely in their spatial positions, the average value of the PS points within 200 m of each GNSS station was used as the InSAR observation value associated with that station. As can be seen in Table 3, the absolute error range of the two observation methods was 5.73–7.78 mm/yr, and the average absolute error was 6.860 mm/yr, indicating that the two observation results have high consistency. By comprehensively analyzing the error value of the deformation rate of each NEU component of the GNSS observation results and the accuracy of the deformation rate, we believe that the GNSS observation results in our study can truly reflect the surface deformation in the Beijing Plain area.

Table 3. Vertical cross-validation of GNSS and PS-InSAR.

Station	GNSS (mm/yr)	InSAR (mm/yr)	Absolute Error (mm/yr)	Time Span	Number of InSAR Images
cylg	−35.439	−43.220	7.781	20 May 2017 to 11 January 2021	37
nlsh	1.903	−3.823	5.726	20 May 2017 to 16 February 2021	38
sysg	−15.419	−22.493	7.074	20 May 2017 to 4 May 2020	31

4. Discussion

4.1. GNSS Velocity Field Time Series Variation Characteristic

We took 3 years as a sliding window to fit the velocity estimate of the GNSS stations in each time period. Taking the BJNM station as an example, the average observation velocities for 2011, 2012, and 2013 were used to represent the velocity value of the station in 2012. The results are shown in Figure 5. The length and direction of the red line in the figure represent the speed and direction of the measuring station in the horizontal direction, respectively, while the length and direction of the black line represent the deformation rate and direction of the station in the U component, respectively. The horizontal component of the BJNM station in Figure 5a indicates that the motion direction is close to SE–SEE, with a velocity of about 5 mm/yr. The U component indicates vertical surface uplift, with a rate of about 2 mm/yr.

It can be seen in Figure 5a,f that the vertical changes of the BJNM, DAXN, XIJI, CPXT, and SYSG stations presented no uniform movement trend. Meanwhile, since 2014, the vertical velocity of the CYLG, DSQI, CHAO, PING, and NLSH stations gradually decreased; in particular, since 2018, the vertical velocity of the CYLG and NLSH stations decreased sharply (Figure 5b–d). On the contrary, the vertical velocity of the TZMJ station gradually increased from 2012 to 2017 (Figure 5d), and the vertical velocity of the HBZS and LLHS stations gradually changed from uplift to subsidence (Figure 5e). The velocity of vertical motion varied greatly among these stations, reflecting the inhomogeneous subsidence in the plain area.

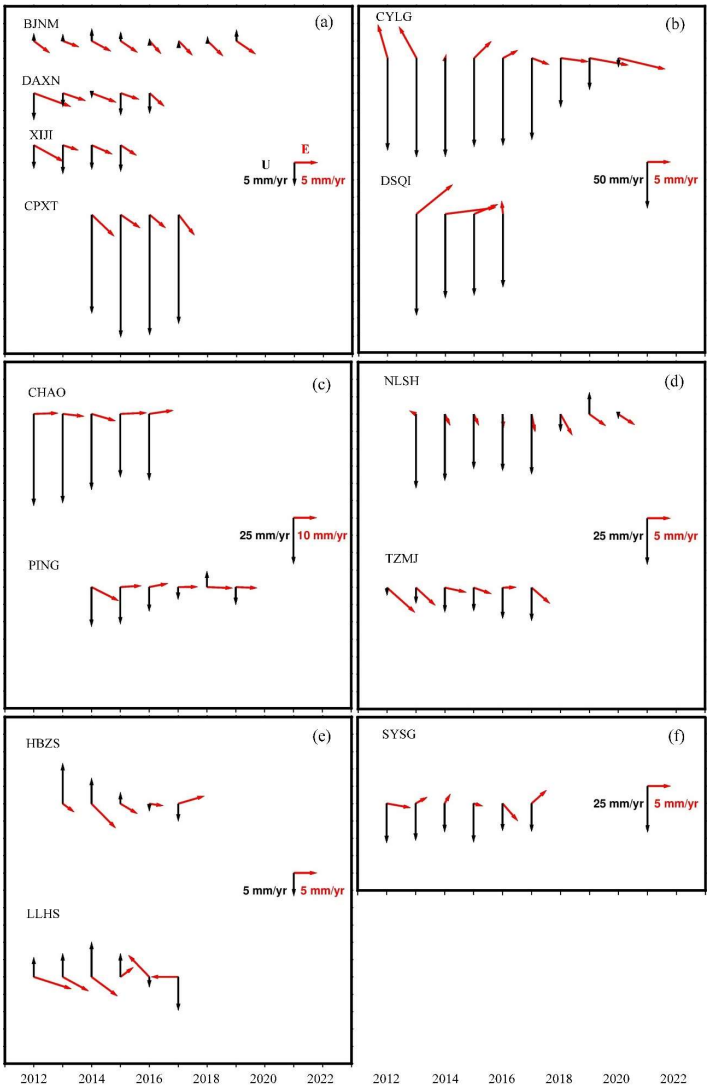

Figure 5. Time-series variation trend of the GNSS velocity field at several stations from 2011 to 2021. The length and direction of the red line in the figure represent the speed and direction of the measuring station in the horizontal direction, respectively, while the length and direction of the black line represent the deformation rate and direction of the station in the U component, respectively (for a more detailed explanation, please see Section 4.2).

As can be seen in Figure 5a that the vertical rate change for the BJNM, DAXN, CPXT, and XIJI stations was small (<5 mm/yr) over the whole time span, corresponding to the magnitude and direction of the horizontal composite vectors with no significant change. However, for the remaining stations (Figure 5b–f), as the vertical velocity of the stations gradually changed, the horizontal composite vectors also changed. Among these stations, the most obvious ones are the CYLG, DSQI, and NLSH stations. With the gradual decrease in vertical velocity, the direction and magnitude of horizontal motion also changed dramatically. Moreover, the horizontal motion direction of the CYLG and NLSH stations gradually tended to match the overall motion direction of the Beijing Plain (SEE direction). In addition, with the gradual change in the vertical motion direction and velocity of the HBZS and LLHS measuring stations, although the change in their velocity values was small, the direction of their horizontal velocity also changed significantly. When calculating the GNSS velocity field in mainland China, Wang and Shen [5] have abandoned some velocity anomaly stations caused by human activities (land subsidence caused by pumping). By comparing their data with the land subsidence map of the Beijing area obtained in this study (Figure 4), it can be proved that all their GNSS stations were outside of the land

subsidence area, and the horizontal velocity reflects the motion state of the Beijing Plain under the stable Eurasian framework.

In summary, based on the three-dimensional deformation characteristics observed using GNSS in our study and the solution strategy proposed by Wang and Shen [5], we believe that land subsidence can affect the horizontal velocity of the GNSS, potentially even changing its direction.

4.2. Physical Mechanism of Land Subsidence Affecting GNSS Horizontal Velocity Field

According to the formation factors, land subsidence can be divided into natural factors and human factors [16]. The natural factors include tectonic movement, stratigraphic structure, stratigraphic lithology, groundwater structure, and so on. For example, during the Quaternary period, the Nankou–Sunhe fault was strongly active in the Beijing area (with northeast wall uplift and southwest wall subsidence in the northwest section of the fault; northeast wall subsidence and southwest wall uplift in the southeast section of the fault), and the Shahe depression and Shunyi depression formed on both sides of the fault [39]. Human factors mainly derive from human activities, including groundwater extraction, oil recovery, mining, and construction loading [5,19]. As we all know, Beijing is the capital of China, and our study area is concentrated in the urban area, so there is no mining and oil extraction area; therefore the exploitation of oil and ore is not the reason for the land subsidence in the Beijing Plain. A relevant study showed that the contribution rate of the construction load to land subsidence in the Beijing Plain is only 13.46% [19]. A large number of studies have shown that the land subsidence in Beijing is mainly caused by the consolidation and compaction of underground compressible layer groups due to excessive groundwater extraction [40,41].

Based on the displacement field caused by the strain in an infinitesimal volume in a uniform elastic half-space, Rothenburg et al. [42] estimated the ground motion and horizontal stress caused by the drop of pore pressure by pumping. Their results also proved that pumping caused land subsidence, where the subsidence magnitude gradually decreased from the pumping center outward (Figure 6a). At the same time, horizontal strain also occurs on the surface of the subsidence area, and its displacement toward the subsidence center—as well as the maximum horizontal strain—is close to the maximum curvature of the subsidence profile (Figure 6b). From the measured data and theory, Burbey et al. [43] and Burbey [44] have also shown that pumping can cause local vertical and horizontal deformations. The formation mechanism of the research on the surface horizontal movement caused by pumping is mainly based on the simply supported beam theory [45]; that is, the drainage of pore water in the underground porous medium caused by pumping leads to uneven vertical compression deformation of the compressible layer group. The overlying strata, in order to respond to the uneven vertical consolidation compaction of the compressible layer, undergoes uneven subsidence not only in the vertical direction but also in the horizontal direction, resulting in horizontal displacement toward the subsidence center (Figure 6c). As shown in Figure 6d, point A is located at the critical position between the subsidence zone and the non-subsidence zone. When point B at the subsidence center settles to point B′, the distance between A and B changes from AB to AB′ and becomes significantly longer, indicating that the material between A and B is displaced towards the subsidence center due to the influence of tensile tension between A and B.

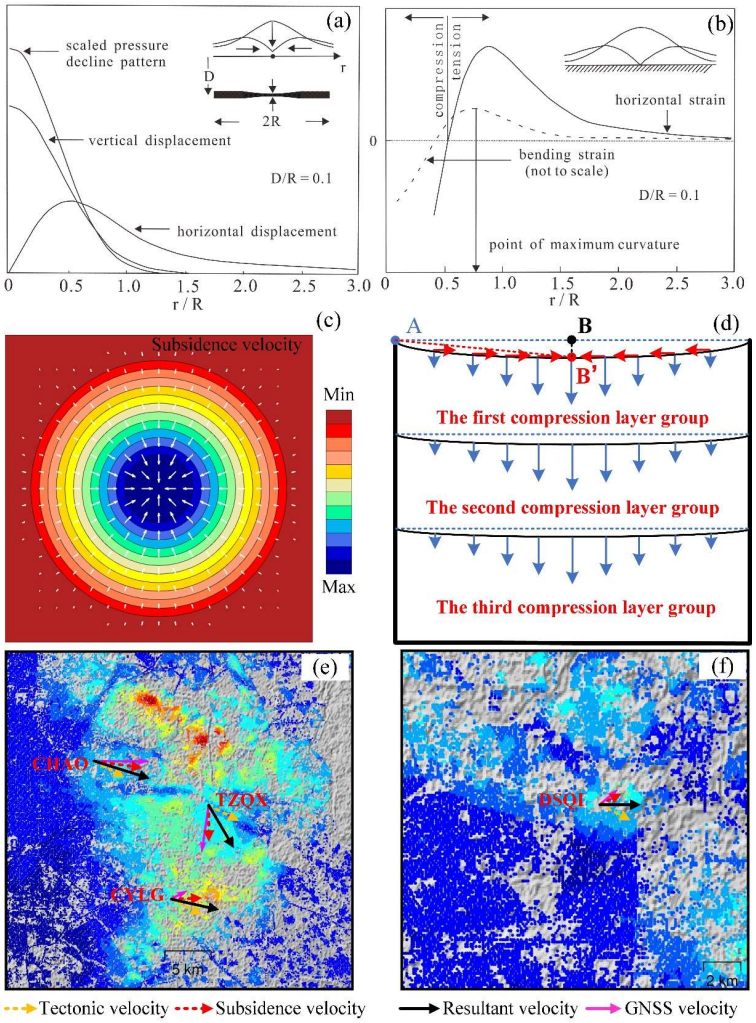

Figure 6. Particle movement direction in the subsidence area: (**a**) Horizontal and vertical displacement of surface caused by pumping; (**b**) subsidence profile curvature and horizontal strain; (**c**) top view, white arrow represents horizontal movement direction of particle, background is subsidence rate diagram; (**d**) profile view, red arrow indicates horizontal motion direction of particle, blue arrow indicates vertical motion direction of particle; and (**e**,**f**) horizontal movement direction of GNSS stations in the study area. Note: (**a**,**b**) were modified from Rothenburg et al. (1995).

In summary, we considered that the GNSS horizontal velocity field of the subsidence area in the Beijing Plain is affected by both regional tectonics and local subsidence. In Figure 6e,f, the orange dotted arrow represents the velocity field under the action of regional tectonic movement in the Beijing Plain region, while the red dotted arrow represents the velocity field under the action of local subsidence of GNSS stations (i.e., toward the subsidence center). The resultant velocity of the two should be the theoretical velocity of GNSS stations. However, this is slightly different from the actual GNSS velocity field that we actually observed. The main reasons for this may be as follows: First, when the horizontal deformation field caused by pumping is studied, based on the theoretical model, the horizontal deformation field is a symmetrical circle (or ellipse) shape and, after being superimposed on the vertical subsidence, the whole three-dimensional deformation field presents a "bowl" shape [42,46]; however, in the Beijing Plain area, the subsidence area and subsidence velocity are irregular, which indicates that the horizontal deformation caused by subsidence may not move completely toward the subsidence center. Therefore, the actual GNSS observed velocity direction deviates from the theoretical regional horizontal velocity direction. Another point is that it is affected by the different time spans of the original observed data. The time spans of the observed InSAR and GNSS data collected in

our study are not completely consistent, resulting in a certain spatio-temporal deviation between the horizontal velocity field observed by the GNSS and the subsidence center observed by the InSAR. However, there is no doubt that the land subsidence process will indeed affect the local GNSS horizontal velocity field.

The CYLG monitoring station located in the eastern plain area of Beijing is near the subsidence funnel, with an average subsidence rate of −82.42 mm/yr. Due to the inflow of southern water into Beijing and the implementation of water control and water-saving policies in Beijing (e.g., the closing of self-provided wells, ecological water replenishment, and the use of reclaimed water; see http://www.beijing.gov.cn/ywdt/zybwdt/202107/t20210720_2444760.html (accessed on 15 October 2022), the vertical velocity of the CYLG station gradually decreased from −100.03 mm/yr in 2012 to −9.79 mm/yr in 2020 and, correspondingly, its horizontal movement direction has gradually changed from NW-trending in 2012 to SEE-trending, thus approaching the regional velocity field (Figure 5b). In the Niulanshan area, located in the Chaobai River Basin, the land subsidence rate has gradually slowed down due to groundwater recharge over the years [47]. This is well-confirmed by the GNSS monitoring results. The vertical motion rate of the NLSH station in the region gradually decreased from −40.07 mm/yr in 2013 to −2.43 mm/yr in 2020, and there was a small surface uplift in 2019. Accordingly, its horizontal motion direction has gradually changed from the NW direction in 2013 to the southeast direction, again approaching the regional velocity field (Figure 5d). In addition, the vertical rates of the CHAO, DSQI, and PING stations also gradually decreased after 2014 (Figure 5b,c). However, during the effective observation period of our GNSS, the land subsidence rates at the stations were still relatively high, indicating that these stations are still affected by local subsidence. Therefore, the horizontal velocity has not recovered to the direction of the regional velocity field (SEE direction); however, the land subsidence of Beijing has developed for many years and is distributed in multiple areas in the Beijing Plain area. Some areas are still experiencing accelerating subsidence (e.g., TZMJ station) or gradually forming new subsidence areas (e.g., HBZS and LLHS station), providing a challenge for the prevention and control of land subsidence in Beijing.

In the future, we believe that, when using the GNSS horizontal velocity field to study regional tectonic dynamics, the geological environment of the station and whether the horizontal velocity can truly reflect the regional tectonic strain field should be carefully considered. The subduction and collision of the Indian plate towards Eurasia not only caused the uplift of the Tibetan Plateau but also made the northeastern margin of the Tibetan Plateau continue to move in the northeast direction, resulting in the overall movement of the north China plate, where the Beijing Plain is located, in the SEE direction [48]. Therefore, under the stable Eurasian framework, the observed data in our study and the recently released velocity field data in mainland China [5] indicate that the horizontal deformation field in the Beijing Plain area is mainly caused by the tectonic activity-derived overall SEE-direction movement, while GNSS horizontal velocity field anomalies are caused by land subsidence in local areas.

5. Conclusions

In this paper, we used GNSS data from 2011 to 2021 and Sentinel 1A data from 2017 to 2021 to discuss whether land subsidence affects the regional GNSS horizontal velocity field in the Beijing Plain area. Some conclusions are as follows:

(1) Compared to the stable Eurasian framework, the GNSS stations range from −1.32 to 10.41 mm/yr in the E component and from −8.83 to 3.00 mm/yr in the N component, presenting obvious inconsistencies. From 2011 to 2021, there was significant uneven land subsidence in the Beijing Plain area, where the severe land subsidence areas were mainly located at the junction of Chaoyang and Tongzhou, the south of the Changping District, and the north of the Haidian District. The maximum land subsidence rate reached 107 mm/yr during the period of 2017 to 2021.

(2) Land subsidence indeed affects the GNSS horizontal velocity field in the subsidence area; under the EURA_I08 reference frame, the horizontal deformation field in the Beijing Plain area was mainly caused by the tectonic activity-derived overall SEE-direction movement, accompanied by velocity field anomalies caused by local land subsidence.

(3) Due to the implementation of the south-to-north water diversion project and the policy of water control and replenishment, the storage structure of the groundwater in Beijing has changed, and the velocity of local land subsidence has gradually slowed down. With this shift, the horizontal velocities of some GNSS stations located in the subsidence area have gradually tended toward the regional velocity field.

The conclusions of our study can provide reference for researchers using GNSS to study seismic geology. Due to the low density of the GNSS stations, there were few GNSS stations in the land subsidence areas, and the considered time span was not long enough. For future research, we plan to collect more data from stations over a longer time span in order to obtain more comprehensive results.

Author Contributions: All authors collaborated to conduct this study. J.W., scientific analysis, manuscript writing, and editing. S.H. and Z.Y., experimental design, project management, and review and editing. T.W. and H.L., review and editing. All authors have read and agreed to the published version of the manuscript.

Funding: This research was financially supported by the National Natural Science Foundation of China (No. 42271082) and the Open Foundation of the United Laboratory of Numerical Earthquake Forecasting (Grant No: 2021LNEF01).

Data Availability Statement: The Sentinel 1A data can be downloaded at https://search.asf.alaska.edu/ (accessed on 1 June 2022).

Acknowledgments: We thank all editors and reviewers for their valuable comments and suggestions, which improved this manuscript. The figures in this paper were made using GMT and ArcGIS.

Conflicts of Interest: The authors declare no conflict of interest.

References

1. Altamimi, Z.; Rebischung, P.; Métivier, L.; Collilieux, X. ITRF2014: A new release of the International Terrestrial Reference Frame modeling nonlinear station motions. *J. Geophys. Res. Solid Earth* **2016**, *121*, 6109–6131. [CrossRef]
2. Han, C.; Liu, L.; Cai, Z.; Lin, Y. The space–time references of BeiDou Navigation Satellite System. *Satell. Navig.* **2021**, *2*, 1–10. [CrossRef]
3. Cheng, P.; Cheng, Y.; Wang, X.; Xu, Y. Update China geodetic coordinate frame considering plate motion. *Satell. Navig.* **2021**, *2*, 1–12. [CrossRef]
4. HU, S.; Wang, T.; Guan, Y.; Yang, Z. Analyzing the seasonal fluctuation and vertical deformation in Yunnan province based on GPS measurement and hydrological loading model. *Chin. J. Geophys.* **2021**, *64*, 2613–2630.
5. Wang, M.; Shen, Z.K. Present-day crustal deformation of continental China derived from GPS and its tectonic implications. *J. Geophys. Res. Solid Earth* **2020**, *125*, e2019JB018774. [CrossRef]
6. Müller, M.D.; Geiger, A.; Kahle, H.G.; Veis, G.; Billiris, H.; Paradissis, D.; Felekis, S. Velocity and deformation fields in the North Aegean domain, Greece, and implications for fault kinematics, derived from GPS data 1993-2009. *Tectonophysics* **2013**, *34–49*, 597–598. [CrossRef]
7. Lazos, I.; Papanikolaou, I.; Sboras, S.; Foumelis, M.; Pikridas, C. Geodetic Upper Crust Deformation Based on Primary GNSS and INSAR Data in the Strymon Basin, Northern Greece—Correlation with Active Faults. *Appl. Sci.* **2022**, *12*, 9391. [CrossRef]
8. Zheng, G.; Wang, H.; Wright, T.J.; Lou, Y.; Zhang, R.; Zhang, W.; Shi, C.; Huang, J.; Wei, N. Crustal deformation in the India-Eurasia collision zone from 25 years of GPS measurements. *J. Geophys. Res. Solid Earth* **2017**, *122*, 9290–9312. [CrossRef]
9. Chen, K.; Avouac, J.-P.; Aati, S.; Milliner, C.; Zheng, F.; Shi, C. Cascading and pulse-like ruptures during the 2019 Ridgecrest earthquakes in the Eastern California Shear Zone. *Nat. Commun.* **2020**, *11*, 1–8. [CrossRef]
10. Lyu, M.; Chen, K.; Xue, C.; Zang, N.; Zhang, W.; Wei, G. Overall subshear but locally supershear rupture of the 2021 Mw 7.4 Maduo earthquake from high-rate GNSS waveforms and three-dimensional InSAR deformation. *Tectonophysics* **2022**, *839*, 229542. [CrossRef]
11. Chen, K.; Ge, M.; Babeyko, A.; Li, X.; Diao, F.; Tu, R. Retrieving real-time co-seismic displacements using GPS/GLONASS: A preliminary report from the September 2015 M w 8.3 Illapel earthquake in Chile. *Geophys. J. Int.* **2016**, *206*, 941–953. [CrossRef]

12. Wilkinson, M.W.; McCaffrey, K.J.W.; Jones, R.R.; Roberts, G.P.; Holdsworth, R.E.; Gregory, L.C.; Walters, R.J.; Wedmore, L.; Goodall, H.; Iezzi, F. Near-field fault slip of the 2016 Vettore Mw 6.6 earthquake (Central Italy) measured using low-cost GNSS. *Sci. Rep.* **2017**, *7*, 1–7. [CrossRef] [PubMed]
13. Sboras, S.; Lazos, I.; Mouzakiotis, E.; Karastathis, V.; Pavlides, S.; Chatzipetros, A. Fault modelling, seismic sequence evolution and stress transfer scenarios for the July 20, 2017 (M W 6.6) Kos–Gökova Gulf earthquake, SE Aegean. *Acta Geophys.* **2020**, *68*, 1245–1261. [CrossRef]
14. Shen, Z.K.; Zhao, C.; Yin, A.; Li, Y.; Jackson, D.D.; Fang, P.; Dong, D. Contemporary crustal deformation in east Asia constrained by Global Positioning System measurements. *J. Geophys. Res. Solid Earth* **2000**, *105*, 5721–5734. [CrossRef]
15. Wu, B. Research on the characteristics of crustal deformation in Bohai Rim Region. *Chin. Acad. Surv. Mapp.* **2015**, 49–50.
16. Chen, C. Characteristics of Segmentary Motion and Deformation along the Zhangjiakou-Bohai Fault. *Earthquake* **2016**, *36*, 1–11.
17. Chen, C. Study on Deformation Characteristics and Current Activity State of Crustal Structure in Beijing and Its Adjacent Areas. *Institude Earthq. Sci. China Earthq. Adm.* **2017**.
18. Lei, K.; Ma, F.; Chen, B.; Luo, Y.; Cui, W.; Liu, H.; Tian, F. The three-dimensional (3D) surface displacement in Beijing plain based on time series InSAR and GPS technologies. *J. Eng. Geol.* **2022**, *30*, 417–431.
19. Zhou, C.; Gong, H.; Chen, B.; Li, X.; Li, J.; Wang, X.; Gao, M.; Si, Y.; Guo, L.; Shi, M. Quantifying the contribution of multiple factors to land subsidence in the Beijing Plain, China with machine learning technology. *Geomorphology* **2019**, *335*, 48–61. [CrossRef]
20. Tian, F.; Guo, M.; Luo, Y.; Zhou, Y.; Jia, S. The deformation behavior of soil mass in the subsidence area of Beijing. *Geol. China* **2012**, *39*, 236–242.
21. Cigna, F.; Tapete, D. Present-day land subsidence rates, surface faulting hazard and risk in Mexico City with 2014–2020 Sentinel-1 IW InSAR. *Remote Sens. Environ.* **2021**, *253*, 112161. [CrossRef]
22. Sato, H.P.; Abe, K.; Ootaki, O. GPS-measured land subsidence in Ojiya city, Niigata prefecture, Japan. *Eng. Geol.* **2003**, *67*, 379–390. [CrossRef]
23. Baldi, P.; Casula, G.; Cenni, N.; Loddo, F.; Pesci, A. GPS-based monitoring of land subsidence in the Po Plain (Northern Italy). *Earth Planet. Sci. Lett.* **2009**, *288*, 204–212. [CrossRef]
24. Shi, M.; Gong, H.; Gao, M.; Chen, B.; Zhang, S.; Zhou, C. Recent ground subsidence in the North China Plain, China, revealed by sentinel-1A datasets. *Remote Sens.* **2020**, *12*, 3579. [CrossRef]
25. Sun, H.; Zhang, Q.; Zhao, C.; Yang, C.; Sun, Q.; Chen, W. Monitoring land subsidence in the southern part of the lower Liaohe plain, China with a multi-track PS-InSAR technique. *Remote Sens. Environ.* **2017**, *188*, 73–84. [CrossRef]
26. Saleh, M.; Masson, F.; Mohamed, A.-M.S.; Boy, J.-P.; Abou-Aly, N.; Rayan, A. Recent ground deformation around lake Nasser using GPS and InSAR, Aswan, Egypt. *Tectonophysics* **2018**, *744*, 310–321. [CrossRef]
27. Rateb, A.; Abotalib, A.Z. Inferencing the land subsidence in the Nile Delta using Sentinel-1 satellites and GPS between 2015 and 2019. *Sci. Total Environ.* **2020**, *729*, 138868. [CrossRef]
28. Williams, S.D.; Bock, Y.; Fang, P.; Jamason, P.; Nikolaidis, R.M.; Prawirodirdjo, L.; Miller, M.; Johnson, D.J. Error analysis of continuous GPS position time series. *J. Geophys. Res. Solid Earth* **2004**, *109*. [CrossRef]
29. Altamimi, Z.; Métivier, L.; Collilieux, X. ITRF2008 plate motion model. *J. Geophys. Res. Solid Earth* **2012**, *117*. [CrossRef]
30. Hu, L.; Dai, K.; Xing, C.; Li, Z.; Tomás, R.; Clark, B.; Shi, X.; Chen, M.; Zhang, R.; Qiu, Q. Land subsidence in Beijing and its relationship with geological faults revealed by Sentinel-1 InSAR observations. *Int. J. Appl. Earth Obs. Geoinf.* **2019**, *82*, 101886. [CrossRef]
31. Colesanti, C.; Ferretti, A.; Novali, F.; Prati, C.; Rocca, F. SAR monitoring of progressive and seasonal ground deformation using the permanent scatterers technique. *IEEE Trans. Geosci. Remote Sens.* **2003**, *41*, 1685–1701. [CrossRef]
32. Bekaert, D.; Hooper, A.; Wright, T. A spatially variable power law tropospheric correction technique for InSAR data. *J. Geophys. Res. Solid Earth* **2015**, *120*, 1345–1356. [CrossRef]
33. Bekaert, D.; Walters, R.; Wright, T.; Hooper, A.; Parker, D. Statistical comparison of InSAR tropospheric correction techniques. *Remote Sens. Environ.* **2015**, *170*, 40–47. [CrossRef]
34. Foumelis, M.; Blasco, J.M.D.; Desnos, Y.-L.; Engdahl, M.; Fernández, D.; Veci, L.; Lu, J.; Wong, C. ESA SNAP-StaMPS integrated processing for sentinel-1 persistent scatterer interferometry. In Proceedings of the IGARSS 2018–2018 IEEE International Geoscience and Remote Sensing Symposium, Valencia, Spain, 22–27 July 2018; pp. 1364–1367.
35. Hooper, A.; Bekaert, D.; Spaans, K.; Arıkan, M. Recent advances in SAR interferometry time series analysis for measuring crustal deformation. *Tectonophysics* **2012**, *514*, 1–13. [CrossRef]
36. Zhang, S.; Song, M.; Luo, Y.; Lei, K.; Liu, W.; Pang, X. Research on tropospheric correction for time series InSAR. *Sci. Surv. Mapp.* **2021**, *46*, 108–117.
37. Yu, C.; Li, Z.; Penna, N.T.; Crippa, P. Generic atmospheric correction model for interferometric synthetic aperture radar observations. *J. Geophys. Res. Solid Earth* **2018**, *123*, 9202–9222. [CrossRef]
38. Lin, X. Stability analysis of Beijing leveling origin. *Sci. Surv. Mapp.* **1994**, *03*, 24–27.
39. Huang, X.; Wang, L.; Xu, J.; Fang, Z. Characteristics of neotectonic movement in Beijing area. *Seismol. Geol.* **1991**, *13*, 43–51.
40. Chen, B.; Gong, H.; Chen, Y.; Li, X.; Zhou, C.; Lei, K.; Zhu, L.; Duan, L.; Zhao, X. Land subsidence and its relation with groundwater aquifers in Beijing Plain of China. *Sci. Total Environ.* **2020**, *735*, 139111. [CrossRef]

41. Guo, L.; Gong, H.; Li, J.; Zhu, L.; Xue, A.; Liao, L.; Sun, Y.; Li, Y.; Zhang, Z.; Hu, L. Understanding uneven land subsidence in Beijing, China, using a novel combination of geophysical prospecting and InSAR. *Geophys. Res. Lett.* **2020**, *47*, e2020GL088676. [CrossRef]
42. Rothenburg, L.; Obah, A.; El Baruni, S. Horizontal ground movements due to water abstraction and formation of earth fissures. *Int. Assoc. Hydrol. Sci.* **1995**, *234*, 239–249.
43. Burbey, T.J.; Warner, S.M.; Blewitt, G.; Bell, J.W.; Hill, E. Three-dimensional deformation and strain induced by municipal pumping, part 1: Analysis of field data. *J. Hydrol.* **2006**, *319*, 123–142. [CrossRef]
44. Burbey, T.J. Three-dimensional deformation and strain induced by municipal pumping, Part 2: Numerical analysis. *J. Hydrol.* **2006**, *330*, 422–434. [CrossRef]
45. Liu, H. *Horizontal Aquifer Movement Induced from Ground Water Pumping and Its Relation with Ground Fissure*; Chang'an University: Chang'an, China, 2021.
46. Samieie-Esfahany, S.; Hanssen, R.F.; Thienen-Visser, K.; Muntendam-Bos, A. On the effect of horizontal deformation on InSAR subsidence estimates. In Proceedings of the Fringe 2009 Workshop ESA ESRIN, Frascati, Italy, 30 November–4 December 2009; p. 7.
47. Zhu, L.; Gong, H.; Chen, Y.; Wang, S.; Ke, Y.; Guo, G.; Li, X.; Chen, B.; Wang, H.; Teatini, P. Effects of Water Diversion Project on groundwater system and land subsidence in Beijing, China. *Eng. Geol.* **2020**, *276*, 105763. [CrossRef]
48. Wang, W.; Zhao, B.; Qiao, X.; Ding, K. Block kinematics in North China from GPS measurements. *Geochem. Geophys. Geosystems* **2022**, *23*, e2021GC010216. [CrossRef]